

Unraveling the role of feed temperature and cross-flow velocity on organic fouling in membrane distillation using response surface methodology

Original

Unraveling the role of feed temperature and cross-flow velocity on organic fouling in membrane distillation using response surface methodology / Ricceri, F; Blankert, B; Ghaffour, N; Vrouwenvelder, Js; Tiraferri, A; Fortunato, L. - In: DESALINATION. - ISSN 0011-9164. - 540:(2022), p. 115971. [10.1016/j.desal.2022.115971]

Availability:

This version is available at: 11583/2973554 since: 2022-12-02T07:06:16Z

Publisher:

ELSEVIER

Published

DOI:10.1016/j.desal.2022.115971

Terms of use:

This article is made available under terms and conditions as specified in the corresponding bibliographic description in the repository

Publisher copyright

(Article begins on next page)

1 **Unraveling the role of feed temperature and cross-flow velocity on organic fouling in**
2 **membrane distillation using response surface methodology**

3

4 Francesco Ricceri^a, Bastiaan Blankert^b, Johannes S. Vrouwenvelder^b, Alberto Tiraferri^{a*}, Luca
5 Fortunato^{b*}

6

7 ^a Department of Environment, Land and Infrastructure Engineering (DIATI), Politecnico di Torino,
8 Corso Duca degli Abruzzi 24, Turin, 10129, Italy

9 ^b Water Desalination and Reuse Center (WDRC), King Abdullah University of Science and
10 Technology (KAUST), Biological & Environmental Science & Engineering Division (BESE),
11 Thuwal 23955-6900, Saudi Arabia

12

13 * Corresponding authors

14 **Highlights**

- 15 • Feed temperature governs the fouling behaviour more than cross-flow velocity
- 16 • Higher feed temperature increases the fouling accumulation
- 17 • Higher cross-flow velocity decreases the fouling accumulation
- 18 • Feed temperature and cross-flow velocity were statistically significant for the RSM
- 19 • RSM is a powerful tool to assess performance and fouling behaviour in MD

20 **Abstract**

21 Understanding the role of operating condition on fouling development in membrane distillation
22 (MD) is critical for the further optimization of MD technology. In this study, organic fouling
23 development in MD was investigated with a synthetic model solution of humic acid varying the
24 feed inlet temperature from 35 to 65 °C and the cross-flow velocity from 0.21 to 0.42 m/s. For
25 each experiment, the final fouling layer thickness was estimated using optical coherence
26 tomography, a non-invasive imaging technique. The set of experiments was mined to model the
27 initial flux decline, the final flux, and the final foulant thickness responses by central composite
28 design, a useful response surface methodology (RSM) tool. A strong influence on the initial flux
29 was observed by varying feed inlet temperature. The results indicated a linear increment of the
30 fouling thickness by increasing the feed inlet temperatures. Overall, the feed inlet temperature
31 governed both the initial flux decline and the fouling deposition rate. A more complex behaviour
32 was observed by varying the cross-flow velocity. To this extent, higher cross-flow velocities
33 showed a positive effect on the initial flux, which however translated in larger values of the
34 initial flux decline rate. On the other hand, the higher shear stress contributed to a decrease of the
35 final fouling layer thickness. The proposed approach was proven to be a valuable tool to assess
36 the role of the operating conditions on fouling and process performance in MD.

37

38 **Keywords:** Direct contact membrane distillation (DCMD); Membrane fouling; Optical
39 coherence tomography (OCT); Response surface methodology (RSM);

40 **1 Introduction**

41 Membrane distillation is a thermal-based desalination technology which has gained an
42 exponential interest during the last decades [1, 2]. Among all the possible membrane distillation
43 configurations, direct contact membrane distillation (DCMD) is the most compact. Due to its
44 simplicity, this process has been extensively studied at laboratory scale to approach scale-up
45 applications in MD [3-5]. In fact, DCMD does not require an external condenser and it is more
46 suitable for water-based applications than air gap, vacuum, or sweep gas membrane distillation.
47 In DCMD, the hot feed and the cold permeate solutions are in contact with a hydrophobic
48 membrane. Under ideal working conditions, only water vapor passage is allowed through this
49 microporous membrane [6, 7]. However, several operational challenges might cause decrease in
50 productivity or even process failure [8]. According to the type of treated feed solution, three
51 main drawbacks observed in the operational DCMD phase are: (i) pore wetting, (ii) mineral
52 scaling, and (iii) membrane fouling. Wetting mainly occurs when membrane hydrophobicity is
53 reduced, together with the liquid entry pressure, to the point which allows liquid passage through
54 the pores [9, 10]. Wetting is easily induced by amphiphilic molecules, such as surfactants, and it
55 leads to process failure even in a preliminary recovery stage [11, 12]. Mineral scaling is due to
56 crystal formation of salts at the solid membrane interface, initiating a rapid and severe flux
57 decline which can also translate into pore wetting and membrane damage [13]. Membrane
58 fouling leads to flux reduction over time due by accumulation of feed contaminants on the
59 membrane surface [14].

60 With the increasing interest in MD, the number of possible applications has been also expanded.
61 As a thermal-based process, MD has been largely used for desalination to produce high-quality
62 water while concentrating the feed above typical reverse osmosis limits [15]. Recently, DCMD

63 has been also employed for the treatment of challenging wastewater, such as produced water,
64 textile, and pharmaceutical wastewater [16-18]. Within this range of possible applications, recent
65 studies demonstrated how effective pre-treatment strategies and process optimization could
66 highly reduce pore-wetting and mineral scaling propensity [16, 19]. In this context, membrane
67 fouling is still considered one of the main bottlenecks of MD operations [20, 21]. Among
68 different foulant species, humic substances showed particularly high fouling propensity in low-
69 pressure processes due to high adhesion capacity of these compounds on the membranes [22].
70 Humic acids are also the major constituents of natural organic matter, as well as widely present
71 constituents in surface water, groundwater, and seawater [23]. In this study, organic fouling in
72 DCMD was investigated by using humic acid as model compound under accelerated fouling
73 conditions.

74 Optical coherence tomography (OCT) has been recently demonstrated as an effective and
75 versatile tool for fouling characterization. This non-destructive technique enables monitoring the
76 filtration system under continuous operation, providing real-time information of the fouling layer
77 [24, 25]. OCT allows acquiring non-invasively 2D cross-sectional and 3D volumetric images
78 with micron-level resolution without interfering with the membrane operation. Recently, the use
79 of OCT has been employed for studying the fouling behavior in MD when treating textile,
80 pharmaceutical wastewater, and concentrated brines [17, 18, 26]. In these studies, OCT results
81 were efficiently linked to process performance data allowing an in-depth understanding on how
82 fouling and scaling impact the water flux during the DCMD process. However, these literature
83 studies were often limited to narrow ranges of operative conditions in MD. To extend the
84 understanding of fouling under a wider range of temperatures and cross-flow velocities, response
85 surface modeling (RSM) was implemented in this study through Design Expert software [27-29].

86 One of the way to implement RSM is by using central composite design (CCD), an array
87 whereby investigated parameters are efficiently distributed to allow a second-order generalized
88 regression between the experimental results [30, 31]. Recently, RSM combined with CCD has
89 gained a growing interest in membrane process optimization as it is able to consider several
90 variables at the same time with easy evaluation of the generated responses. An interesting
91 application of RSM in MD was developed by Shokrollahi et al., who effectively modeled flux
92 and thermal efficiency for a wide range of interacting parameters [32]. There, numerical
93 modeling with CCD method for flux optimization showed that temperature and module length
94 have the most important influence on MD productivity.

95 In this study, central composite design is implemented to guide the design of MD experiments
96 conducted with different combinations of feed inlet temperature and cross-flow velocity. The
97 experiments are performed with a synthetic model solution of humic acid, where the distillate
98 flux is monitored as a function feed volume concentration factor. Additionally, OCT *in-situ*
99 monitoring is employed to characterize the fouling layer developed at the end of each MD test.
100 The flux performance and fouling data are discussed and critically examined also to assess a
101 valuable experimental based modeling. Therefore, (i) the initial flux decline rate, (ii) the final
102 flux, (iii) the total flux decline, and (iv) the final fouling thickness are applied as responses
103 (dependent variables) in the RSM analysis to investigate the mechanism of fouling and to
104 identify the most suitable DCMD operating conditions. The investigation assesses the role of
105 process parameters and governing factors on fouling in MD, and it proposes the rational
106 deployment of RSM as a tool to move toward scale-up applications.

107 2 Materials and Methods

108

109 2.1 Membrane and Feed composition

110 Accelerated fouling conditions were employed in this study using a synthetic feed solution with
111 an initial humic acid (HA) concentration of 500 mg/L in deionized (DI) water. To enhance the
112 fouling deposition, 20 mM of calcium chloride, CaCl₂, was also added to the feed solution [33].
113 HA and CaCl₂ were purchased from Sigma-Aldrich. The organic compound was received in
114 powder form. The stock solution was prepared by dissolving the chemicals in 600 mL of DI
115 water. The stock was then added, prior to flux stabilization, to the remaining 400 mL of
116 deionized water used as initial feed. Initial volumes of 1 L were thus used for both the feed and
117 permeate solutions, the latter consisting of DI water.

118 A commercially available hydrophobic polytetrafluoroethylene with a polypropylene support
119 (PP-PTFE) membrane (Membrane Solutions corp., US) was used for all the experiments. The
120 membrane characteristics, provided by the manufacturer or obtained in the lab, are listed in Table
121 1. The membrane permeability coefficient was calculated by dividing the experimental water
122 flux by the vapor pressure difference across the membrane (see calculated angular coefficient
123 from Fig S.1).

124 **Table 1.** Porous PP-PTFE membrane characteristics

Data source	Parameter	Units	Value
Provided by the manufacturer	Thickness	µm	174 - 245
	Mean pore size	µm	0.22
	Bubble point	psi	16.0-20.3
From experiments	Membrane permeability coefficient	kg m ⁻² h ⁻¹ bar ⁻¹	143.8

125

126 2.2 MD lab setups

127 All the MD tests were performed in direct contact membrane distillation (DCMD) configuration
128 with a lab-scale batch system. In this process, the feed and permeate streams were circulated
129 counter-currently on their respective sides of the hydrophobic membrane, not enabling liquid
130 passage through the pores. Thanks to the applied thermal gradient, the colder liquid is enriched
131 by the water vapor extracted from the feed stream during the process. Ranges of feed
132 temperature of 35 - 65 °C and feed cross-flow velocity of 0.21 - 0.42 m/s (deriving from a cross-
133 flow rate ranging from 25 to 50 L/h) were investigated in this study. To clearly assess the role of
134 feed parameters on fouling deposition, a constant temperature and cross-flow velocity of 20 °C
135 and 0.1 m/s were maintained in the permeate side. For the same reason, no feed spacer was used.
136 The temperatures in the feed and permeate inlet of the flow cell were maintained constant
137 throughout the experiment using a thermostatic water bath and a chiller (Corio-CD, Julabo,
138 Germany). The heat exchangers were accurately controlled by the temperature sensors integrated
139 in the conductivity meters (TetraCon 325, Xylem Analytics, Germany) located just before the
140 inlet of the flow cell. On the permeate side, purified water with electrical conductivity below 20
141 $\mu\text{S}/\text{cm}$ was used, whereas the initial feed conductivity was $4.2 \pm 0.2 \text{ mS}/\text{cm}$. For each
142 experiment, the permeate conductivity was continuously monitored to ensure no liquid passage
143 during the tests, i.e., no pore wetting. Cross-flow velocity and outlet-temperature were measured
144 by digital cross-flow meters located in proximity of the flow cell outlet. The flux across the
145 membrane was calculated by recording the change in weight of the permeate tank in time
146 through a computer-interfaced balance. All the instruments were digitally connected and
147 controlled by Lab View software. The DCMD flow cell in polymethyl methacrylate was

148 customized to allow *in-situ* characterization with OCT. The flow cell was had dimensions of 10.0
149 $\times 3.3 \times 0.1$ cm (length \times width \times height) for a total active membrane area of 33 cm².

150 **2.3 Design of experiments and statistical analysis**

151 Design Expert software was used to setup and analyze the response surface methodology (RSM)
152 for DCMD experiments. Central composite design (CCD) was applied to define the number of
153 runs needed for the optimization of the variables and responses. Feed inlet temperature and
154 cross-flow velocity were selected as operating factors, while the initial flux decline rate, the final
155 flux, and the final thickness of the fouling layer were selected as responses after a preliminary
156 phase investigation of experimental results. The Supplementary Material appendix presents
157 further details of the applied CCD method and analyses. The selected ranges of investigation for
158 the various factors are reported in Table 2, together with the coded experimental values
159 extrapolated by Design Expert software. The CCD method generated a suggestion for nine total
160 runs, each with a specific combination of values of T_f and CFV. This procedure allowed
161 weighted probing of the entire multidimensional space. The experimental results were used as
162 input data to generate the model for each response according to the best fit. ANOVA was used
163 for the statistical analysis of the results to evaluate the quality of the model.

164 **Table 2.** Experimental design of the selected of operating conditions, representing the range of
165 experimental variables used in the RSM model

Factors	Unit	Minimum	Maximum	Coded low	Coded high	Mean
Temperature	(C°)	35.0	65.0	40.0	60.6	50.0
Cross-flow velocity	(m/s)	0.21	0.42	0.24	0.39	0.31

166 **2.4 Filtration experiments protocol**

167 Fouling experiments consisted of two phases: (i) a stable flux phase and (ii) a fouling phase. The
168 flux was first stabilized using DI water only as feed, without organic foulants (J_0). This stage
169 allowed achievement of the hydrodynamic equilibrium. The fouling phase then started at time
170 zero, when the appropriate amount of organic foulant stock solution was added into the feed
171 tank. This second phase was run until a volume concentration factor of 2.5 was reached, which
172 was always associated with sufficient operational time to obtain a near stable flux and fouling
173 layer thickness. The increment of CaCl_2 concentration during experiments can be considered
174 negligible for any possible effect in the reduction of the feed vapor tension value. For this reason,
175 the flux decrement observed during the fouling tests can be predominantly attributed to foulant
176 deposition.

177 **2.5 Optical coherence tomography (OCT) analysis**

178 A spectral-domain optical coherence tomography (SD-OCT) system Ganymede II from
179 Thorlabs, GmbH (Germany) was used to assess the fouling deposition on the membrane surface
180 under accelerated fouling conditions. The OCT was equipped with a scan lens (LSM 03BB). The
181 OCT probe was positioned on top of middle point of the DCMD module to characterize the
182 fouling layer thickness at the end of each experiment. 3D cross-sectional OCT scans ($666 \text{ pixel} \times$
183 $666 \text{ pixel} \times 1022 \text{ pixel}$) corresponded to $4.0 \text{ mm} \times 4.0 \text{ mm} \times 2.25 \text{ mm}$ (width \times length \times depth).
184 The OCT scans were processed with the FiJi software. Images were filtered to reduce the noise,
185 then the contrast and brightness were adjusted. 3D scans were then visualized by AVIZO (Field
186 Electron and Ion Company, Hillsboro, OR, USA) software and modified for visualization
187 purpose. The fouling layer thickness was calculated using a customized MATLAB code.

188 **3 Results and discussion**

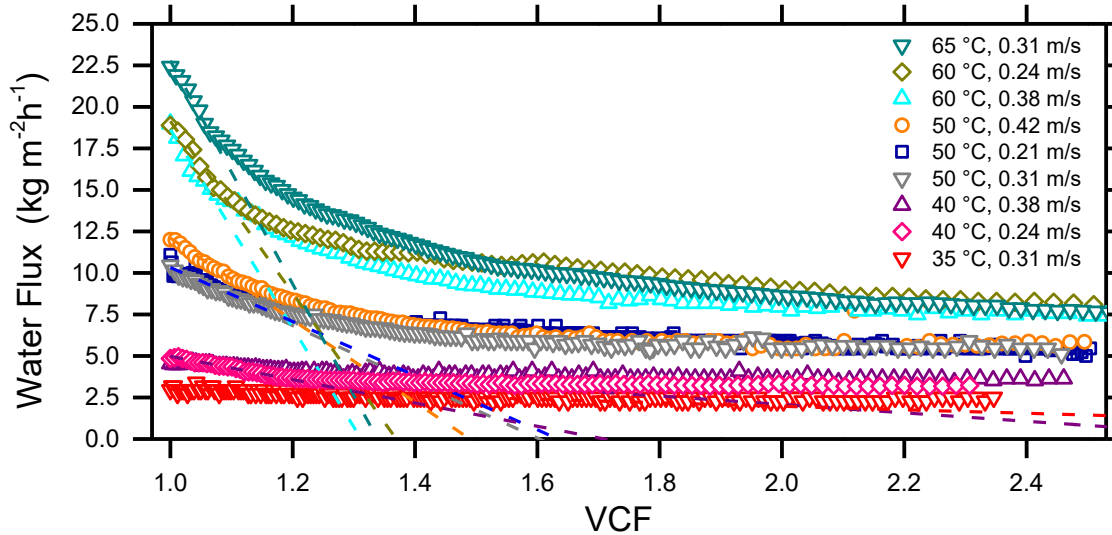
189

190 **3.1 Beyond the RSM: An overall picture of the process parameters in MD organic fouling**

191 **3.1.1 The Effect of temperature and cross-flow velocity on the experimental flux**

192 This section describes the experimental results while providing an in-depth understanding of the
193 selected responses (dependent variables) of the RSM model. In this study, Design Expert was
194 employed as a statistical tool to create the experiment plan aimed at studying the impact of
195 operating condition on the fouling behavior in DCMD. The list of experiments is reported in
196 Table S.1 and in the legend of Fig 1, where experimental results of water production in DCMD
197 at different operating conditions are also shown.

198 In DCMD process, the initial flux, J_0 , is related to the feed temperature and cross-flow velocity
199 [34, 35]. As expected, in this study the inlet feed temperature was found to govern J_0 . By
200 increasing T_f from 35 to 65 °C, the J_0 increased from 3 to 22.5 kg m⁻²h⁻¹, while increasing the
201 cross-flow velocity from 0.21 to 0.42 m/s at fixed T_f 50 °C led to an increase of only 2 kg
202 m⁻²h⁻¹. This result can be attributed to the nature of the driving force, namely, the vapor tension
203 difference between the feed and the permeate, which can be easily determined through Antoine
204 equation [36]. On the other hand, the cross-flow velocity can contribute to the flux increment by
205 reducing the temperature polarization effects [37].



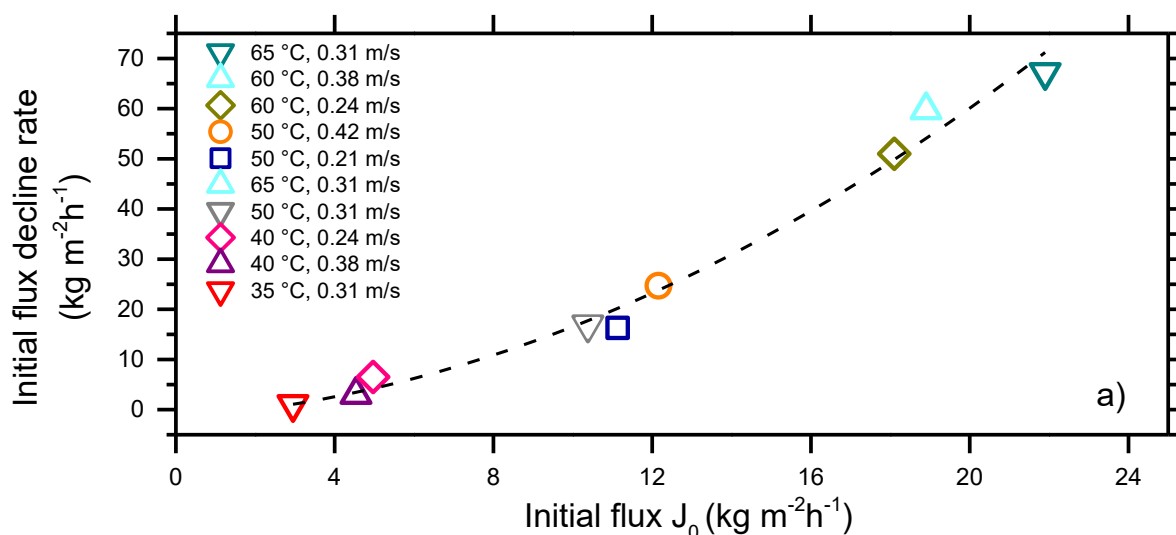
206

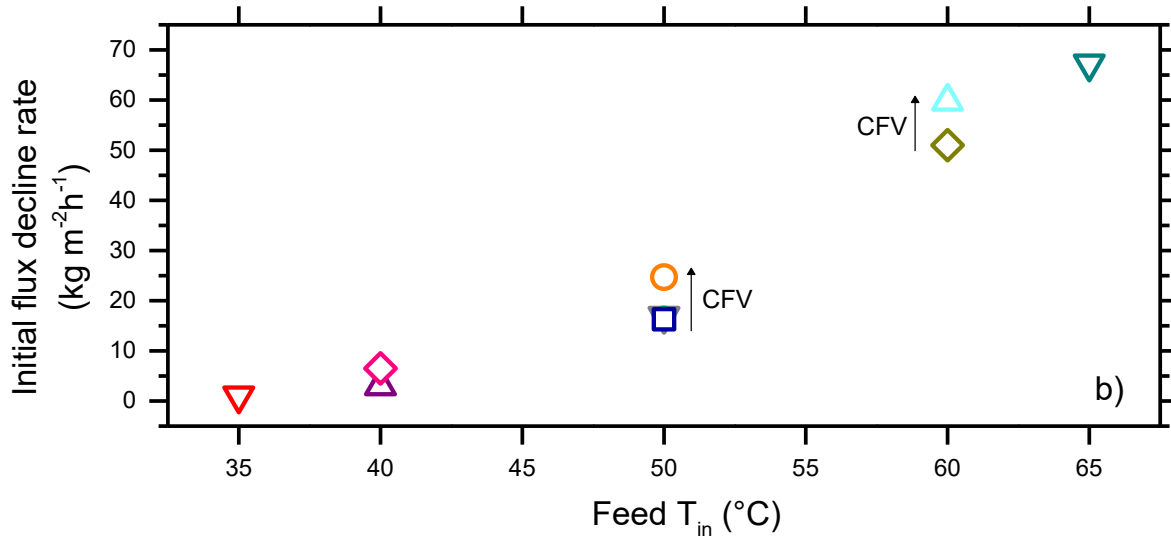
207 **Figure 1.** Results of fouling experiments performed with the synthetic feed water in the
 208 presence of 500 mg/L humic acid and 20 mM of calcium chloride at different initial permeate
 209 flux, J_0 , obtained by changing the applied feed temperature and cross-flow velocity in DCMD.
 210 Water fluxes (J_w) were investigated until a volume concentration factor (VCF) of 2.5 was
 211 reached, at which a value of near-stable final flux was observed for all the experiments. Dash
 212 lines represent the best linear fit of the first 1.25 volume concentration factor (VCF) of the initial
 213 flux decline.

214

215 In all the tests, the water flux decreased almost linearly in the initial phase, to then reach an
 216 approximate flux stabilization over time when the nominal driving force was counterbalanced by
 217 resistances due to fouling accumulation to yield a constant effective driving force [38]. As
 218 fouling deposition is proportional to the water transport across the membrane, high accumulation
 219 typically occurs in the initial phases of operation, contributing to the formation of a cake layer
 220 during this initial stage [39, 40]. The initial flux decline rates were estimated from the best linear

221 fit (see dash lines in Fig 1a) of the water flux measured between 1 and 1.25 VCF. The values are
 222 reported as a function of the initial flux J_0 (Fig 2a) and of the inlet feed temperature (Fig 2b). The
 223 results suggest a smooth and gradually incrementing correlation of the initial flux decline when
 224 increasing J_0 . The proportional effect of J_0 on the initial flux decline has been also widely
 225 investigated in osmotically and pressure-driven membrane processes [41-43]. As expected, an
 226 analogous behavior was observed when looking at the data as a function of the inlet feed
 227 temperature (Fig 2b), as the driving force is closely related to this parameter. The data also allow
 228 assessment of the role of the cross-flow velocity, whose increment seems to slightly affect the
 229 initial flux decline, as an indirect effect of slightly larger values of J_0 observed when increasing
 230 CFV. The values of near stable flux at the end of the tests, J_w , and the ratio J_w / J_0 were also
 231 extrapolated from the flux decline data for each tested condition.





232 **Figure 2.** Plot of the initial flux decline rate as a function of (a) the initial permeate flux J_0 , and
 233 (b) the inlet feed temperature (T_f). The arrows indicate the increment of the cross-flow velocity
 234 (CFV). Data were extrapolated from dash lines rates reported in Fig 1.

235

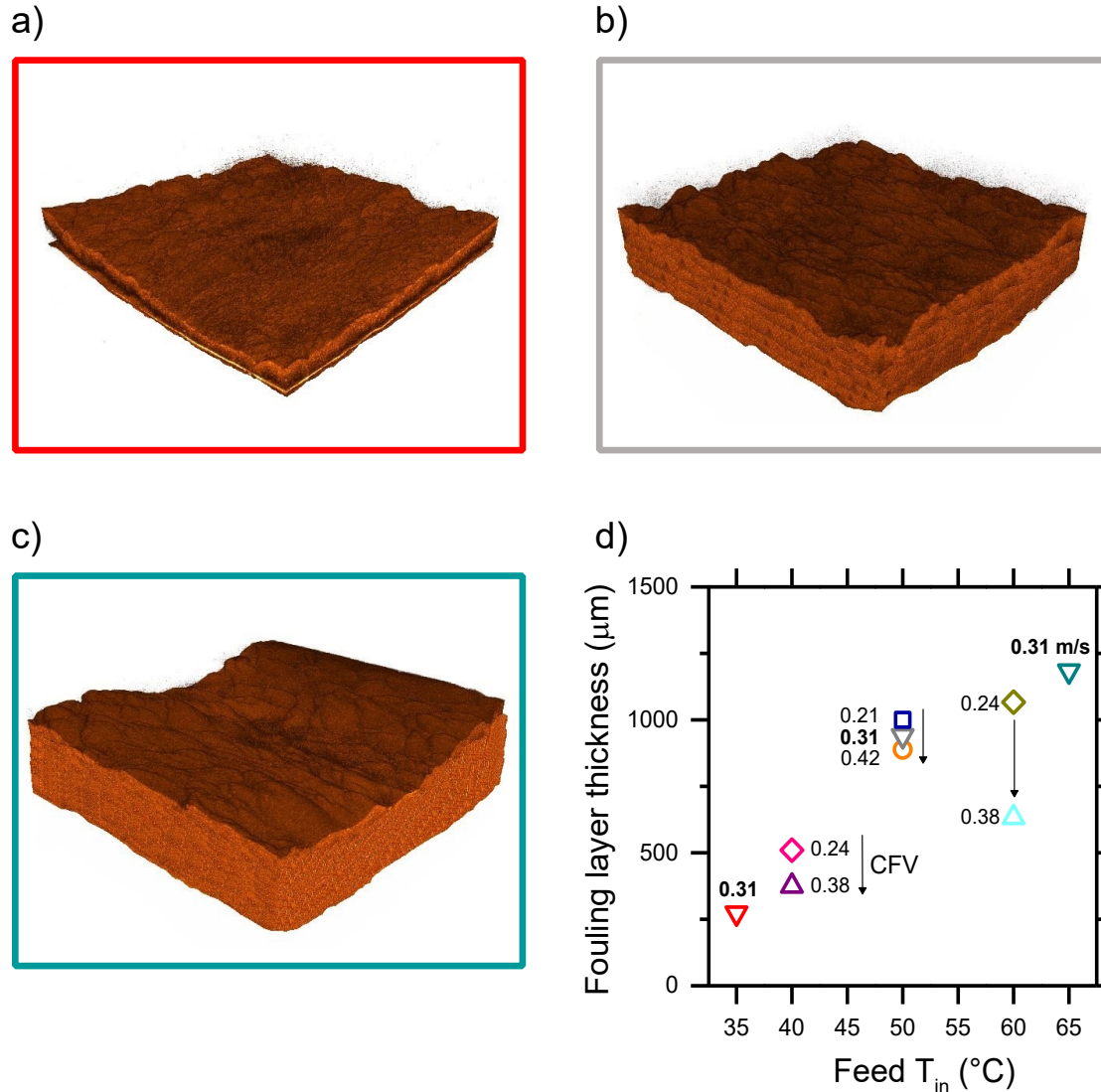
236 A few interesting observations may be made by analyzing the data presented in Figs 1, 2. While
 237 utilizing an inlet feed temperature set at 65 °C produced an initial flux ($22.5 \text{ kg m}^{-2}\text{h}^{-1}$) that is
 238 nine times higher the flux observed with a temperature equal to 35 °C ($2.5 \text{ kg m}^{-2}\text{h}^{-1}$), the flux at
 239 the end of the tests (J_w) was only 3 times larger, reaching roughly $7.5 \text{ kg m}^{-2}\text{h}^{-1}$ for the former
 240 condition, whereas no significant decline in flux was observed at the lower feed temperature.
 241 These results give reasons for operating at low-medium feed temperatures, namely, at or below
 242 50 °C for water streams with high fouling potential and if membrane cleanings are not frequently
 243 operated. In such cases, the long-term productivity may be similar within a wide range of bulk
 244 feed temperature and working at lower temperature would result in savings in terms of energy
 245 demand. This may in turn translate, e.g., into cheaper solar fields with smaller footprints if the

246 energy is harvested from the sun, or anyway into a higher energy efficiency and gain output
247 ration (GOR) value for the overall process.

248 **3.1.2 OCT results for the fouling layer thickness**

249 Water flux data were linked to non-invasive direct fouling characterization performed with OCT
250 to characterize the fouling layer developed on the membrane surface by scanning the central
251 positions of the cell. Please note that the homogeneity of the fouling layer along the membrane
252 length was confirmed by preliminarily evaluating the thickness growth at different positions of
253 the cell. As no spatial gradient was observed, the middle position was selected as a representative
254 location. The 3D OCT rendering images (Fig 3) show the fouling deposition obtained at T_f of 35,
255 50, 65 °C, thus covering the whole range of T_f investigated. The results highlight the increase of
256 the foulant deposition by incrementing the inlet feed temperature. In these three examples, the
257 same cross-flow velocity of 0.31 m/s was applied, representing the central point suggested by
258 Design Expert within the explored CFV range (see Table S.1). In general, a slight increment of
259 the foulant roughness was observed by increasing T_f , as nodule-like and valley-like structures
260 became more pronounced. This phenomenon was also discussed by Laqbaqbi et al. when testing
261 DCMD fouling at a temperature close to 70 °C [44].

262



263 **Figure 3.** 3D OCT rendered scans ($4\text{mm} \times 4\text{mm}$) of the final steady-state foulant layer thickness
 264 from the experiments conducted at cross-flow velocity of 0.31 m/s and feed inlet temperature of
 265 35°C , 50°C , 65°C in (a), (b), (c), respectively. The frame color of the OCT images corresponds
 266 to the color of the associated data points reported in (d). Here, the final thickness is plotted
 267 against the feed inlet temperature for all the tests. The number indicated close to each data point
 268 represents the cross-flow velocity associated with the respective test and expressed in m/s .

269

270 For all the experiments, fouling layer thickness measured with the OCT after 2.5 of volume
271 concentration factor (VCF) is reported in Fig. 3d. In general, a near-linear increment of the
272 thickness was observed as a function of T_f , for the entire investigated range of temperatures.
273 Thus, the thickest deposition was observed for the experiment performed at 65 °C, achieving a
274 layer thickness of almost 1200 μm at the end of the test. A much smaller layer of roughly 200
275 μm was observed with T_f of 35 °C. This last result is in agreement with previous DCMD studies
276 reporting negligible organic fouling with a feed temperature below 40 °C [45]. As opposed to the
277 effect of T_f , higher CFV values were beneficial for reducing the fouling layer development in
278 MD. The arrows in Fig 3d indicate data points associated with different CFV values. As reported
279 in the literature, the increment of the shear stress thwarted foulant accumulation by lowering the
280 boundary layer thickness [46, 47].

281 The results presented imply a strong cause-consequence relation between the operating
282 parameters in MD and fouling development, but without considering how fouling deposition can
283 affect the overall driving force, i.e., the thermal balance during the process. Although the
284 reciprocal influence between the driving force and fouling deposition has been widely
285 investigated for pressure-driven and osmotically-driven processes [43, 48, 49], further research
286 efforts are required to evaluate the interaction between governing factors and fouling in MD. In
287 summary, the *in-situ* observation performed in this study confirmed the link between feed
288 temperature and fouling propensity. The fouling thickness was found to (i) increase with feed
289 inlet temperatures T_f , while (ii) slightly decreasing with cross-flow velocity. The thickness of the
290 fouling layer may thus also be used as a robust response parameter for the RSM analysis
291 discussed below.

292

293 **3.2 Modeling of organic fouling in DCMD through response surface methodology (RSM)**
294

295 **3.2.1 Significance of operating parameters**

296 Organic fouling in DCMD was investigated under different feed inlet temperatures and cross-
297 flow velocities by performing nine DCMD filtration experiments, with combinations of
298 operating parameters suggested by the central composite design approach. Based on the results
299 described above, four parameters were selected as potentially valuable responses for the response
300 surface analysis: (i) initial flux decline rate, (ii) J_w / J_0 value at the end of the test indicating the
301 relative loss of productivity due to fouling, (iii) near-stable flux, (iv) final foulant layer thickness.
302 Experimental results for these parameters were used as input data (responses) to generate the
303 relative model function. According to Design Expert, all these responses were statistically
304 significant to both T_f and CFV, i.e., low p-value. Table 3 summarizes the p-values obtained from
305 ANOVA. Specifically, T_f was found to be considerably more significant than CFV. Each
306 response was fitted by a different model function. The initial flux decline was described by a
307 quadratic model while all the other responses were adequately described by a linear model, as
308 can be seen by the absence of cross-correlation terms in Table 3. Within the three linear
309 responses, CFV was not highly significant, as the p-value was > 0.1 . However, CFV was
310 included in the model to respect the hierarchy of the statistical method and to improve the fit
311 [50]. For each response, the final equation calculated by Design Expert and relating operating
312 parameters with fouling outcomes (responses) is reported in the Supplementary Material
313 appendix (see Table S.2.).

314 **Table 3** Summary of response significance values estimated by ANOVA statistical analysis.

Source	Initial flux decline p-value	Final J_w/J_0 p-value	Final flux p-value	Final thickness p-value
--------	---------------------------------	----------------------------	-----------------------	----------------------------

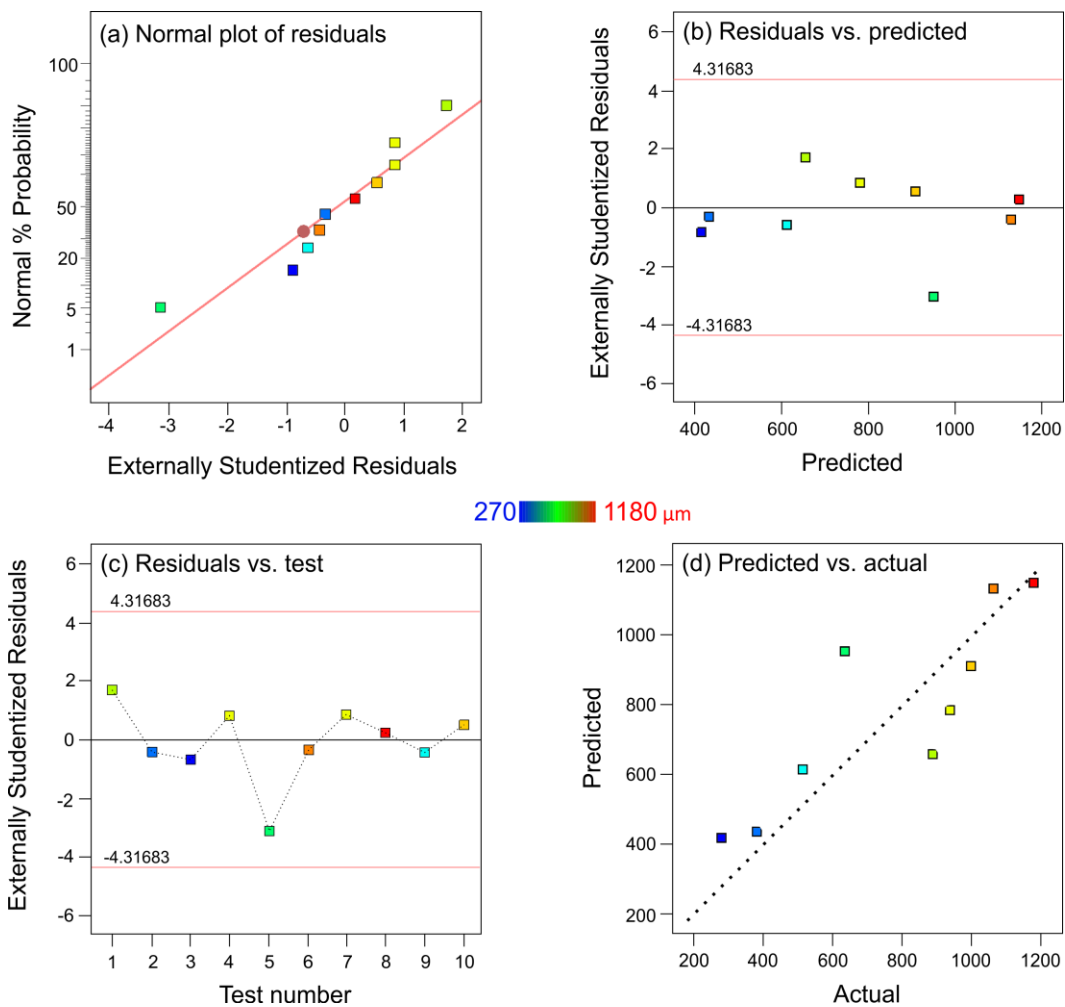
Model	0.0001	0.0004	< 0.0001	0.0133
A-Cross-flow velocity	0.0835	0.4156	0.2145	0.2191
B-Feed temperature	< 0.0001	0.0001	< 0.0001	0.0059
AB	0.0812			
A ²	0.1153			
B ²	0.0017			

315

316 To provide a detailed statistical analysis, the diagnostic plots of the initial flux decline, the final
317 flux, and the final J_w/J_0 values are shown in Fig S.2, S.3 and S.4, respectively. Figure 4 displays
318 the diagnostic plots for the final foulant layer thickness. Please note that the following discussion
319 relates directly to layer thickness, but the conclusions and implications are also valid for the
320 other selected responses. Figure 4a reports the normal probability plot of residuals (error terms),
321 a graphical tool for comparing a data set with the normal distribution: if the data can be
322 adequately described with a normal distribution, characterized by a mean and a variance, then a
323 plot of the theoretical percentiles of the normal distribution versus the observed sample
324 percentiles should be approximately linear. In Fig 4a, the red linear line represents the theoretical
325 normal distribution while the ten dots represent the observed samples (10 runs, Table S1). For all
326 the responses, normal probability plot of the residuals fell on a straight line, which implies that
327 error terms had a normal distribution [51, 52].

328 Figure 4b shows that all points are scattered around the 0 y-axis (variance or standard deviation)
329 reflecting equal or similar variances of collected data. In fact, nine points out of ten lie within
330 two standard deviations, meaning that 95% of values are included in this range (empirical rule).
331 In this case, the variance of residuals can be considered as a constant (homoscedasticity).
332 Homoscedasticity is an important assumption of parametric statistical tests. In Fig. 4c, residuals
333 vs. data points do not follow a specific pattern, which suggests that responses are not dependent
334 on the order of runs. Lastly, Fig. 4d illustrates that predicted values vs. experimental values lay

335 on a straight 45 degree line, an indication of high-quality modeling outcome. In conclusion, the
 336 diagnostic plots of all the responses indicate the robustness of the statistical analysis, which
 337 enable to assess the impact of the operating parameters on the organic fouling behavior in MD.

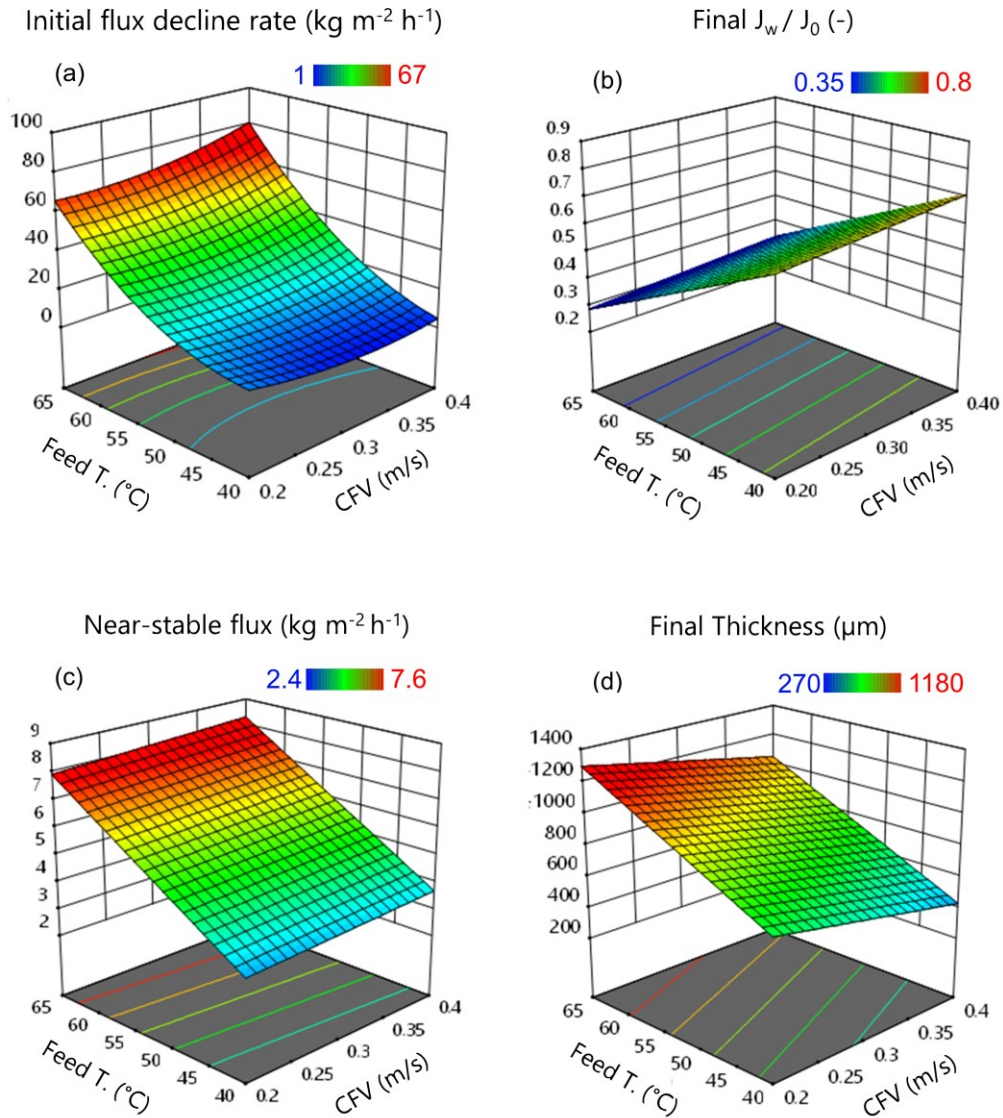


338
 339 **Figure 4.** Diagnostic plots for the foulant layer thickness response: (a) normal % probability vs.
 340 residuals; (b) residuals vs. predicted; (c) residuals vs. run order; (d) predicted vs. actual.

341

342 3.2.2 Single responses evaluation

343 Fig 5 shows the outcome of the RSM model in terms of effects of operating parameters, i.e.,
344 temperature and cross-flow velocity, on the fouling behavior, namely, initial flux decline rate,
345 final J_w/J_0 , the near-stable flux, and the final layer thickness. This discussion aims at providing
346 an effective view of fouling behavior in the whole range of investigated conditions of T_f and
347 CFV and to facilitate any direct comparison among the selected fouling parameters. In
348 accordance with the description in the section above, all the responses were mainly governed by
349 the feed temperature. Specifically, Fig 5b shows how contour values decrease from a J_w / J_0 of
350 0.7 to below 0.3 when the T_f increases from 40 to 65 °C, thus only roughly $1 \text{ kg m}^{-2}\text{h}^{-1}$ of stable
351 flux is gained for each 5 °C-step in ΔT_f (see Fig 5c). As illustrated in Fig 5c, a net increment of
352 the fouling deposition can be observed by increasing T_f , as a twofold increase of layer thickness
353 is associated to an increase of the temperature from 40 to 65 °C.



354

355 **Figure 5.** 2D surface response plots as a function of the feed inlet temperature and cross-flow
 356 velocity for the (a) initial flux decline rate, (b) final to initial flux ration, (c) near-stable flux, and
 357 (d) final foulant layer thickness. The near-stable flux is the flux at volume concentration factor of
 358 2.5 for the experiments reported in Fig 1. The magnitude for each response increases from blue
 359 to red and is also indicated by numeric values for each contour line.

360

361 In contrast to feed inlet temperature, different behaviors were observed by varying the cross-flow
362 velocity. The initial flux decline rate was more affected by the CFV at higher T_f values (see Fig
363 5a). This result can be explained by the proportionality between T_f and temperature polarization
364 (TP) [52]. Faster CFVs thwart TP and this effect is more pronounced when TP tends to be of
365 greater magnitude, that is, at higher values of T_f . This translates into larger J_0 (see Fig 1) and the
366 ensuing steeper flux decline, as observed for CFV values above 0.3 m/s [53, 54]. On the other
367 hand, increasing CFV yielded a positive outcome in terms of productivity when considering the
368 magnitude of the near-stable flux (see Fig 5b, c), likely due to lower fouling deposition
369 associated with smaller boundary layers, as observed in Fig 5c. In fact, the OCT scans
370 highlighted a reduction in fouling layer thickness by increasing the CFV. Interestingly, the CFV
371 was more impactful in decreasing the foulant thickness rather than increasing the overall flux
372 decline J_w / J_0 , implying that foulant thickness and flux loss are not directly correlated but that a
373 complex mechanism is in play. This result might be rationalized with the fact that these two
374 parameters are not independent, for example, J_w may not simply intensify the likelihood of
375 foulant deposition but simultaneously cause enhanced compactness of the resulting layer [55].
376 Both thickness and compactness of the foulant layer play a role in mass and heat transport, and
377 thicker but more porous layer may be less detrimental than thin dense layers that would produce
378 a larger variation in diffusion coefficients and thermal conductivity with respect to the bulk
379 solution.

380 In conclusion, the RSM analysis well depicted the link between fouling propensity and feed
381 temperature, as fouling behavior worsened with the increase of the feed inlet temperature,
382 thereby negatively affecting the flux decline, J_w/J_0 , while a positive but gradually more marginal
383 enhancement of productivity (near-stable flux) was observed when increasing the feed inlet

384 temperature. Moreover, it was found that the increase in cross-flow velocity led to a slight
385 decrease of the fouling thickness deposited on the membrane, while keeping an overall benefit in
386 terms of productivity.

387 **Conclusions**

388 Organic fouling in MD process was investigated using humic acid and calcium chloride in
389 the feed solution. The goal of this study was to assess the role of the feed temperature and
390 cross-flow velocity on fouling behaviour in DCMD. The different operating conditions of the
391 experiments were selected through Design Expert software aiming to build the model
392 function of the selected responses. The four process performance parameters selected as
393 responses (dependent variables) for the RSM were: (i) the initial flux decline rate, (ii) the
394 near-stable flux measured at the end of the tests, (iii) the stable to initial flux ration, J_w / J_0 ,
395 and (iv) the final fouling layer thickness.

396 Higher influence of feed inlet temperature than cross-flow velocity on loss of productivity was
397 observed experimentally and then confirmed by robust statistical analysis, due to the major
398 role of flux in the development of organic fouling in DCMD. In detail, a sharp increment in
399 the overall flux decline, J_w/J_0 occurred at higher feed inlet temperatures, making the case for
400 the need to select an appropriately transmembrane temperature difference that guarantees
401 feasible fluxes but also minimizes loss of driving force and energy demand. The benefits in
402 water productivity obtained by increasing the feed temperature were always offset by higher
403 fouling deposition.

404 Another interesting trade-off between more rapid initial flux decline and thinner layer
405 thickness was observed by increasing cross-flow velocity above 0.3 m/s. Layer thickness is
406 only one of many aspects of the foulant layer that relates to productivity loss, others may
407 include density, pore structure and thermal conductivity, which can directly influence mass
408 and heat transport through this unmixed layer. Optical coherence tomography (OCT) was used
409 in this study to assess layer thickness, but further efforts are needed to deepen investigations

410 on foulant deposition and on how layer characteristics relate to deposition mode and then
411 flux loss. Overall, working at relatively high cross-flow velocity may be beneficial at high
412 values of the nominal driving force, i.e., transmembrane temperature difference, while the
413 results suggest that the effect of channel feed flow velocity may not play a significant role
414 when the flux is below a certain level, approximately $10 \text{ kg m}^{-2}\text{h}^{-1}$.

415 Finally, the proposed approach is not limited to this application but was proven to be a valuable
416 tool to assess the role of the process parameters and governing factors on fouling and process
417 performance in membrane distillation (MD). The results of this study highlight the effectiveness
418 of combining flux data, OCT characterization, and response surface methodology (RSM) to
419 advance the understanding of fouling in MD and open future perspective related to this crucial
420 topic to making MD feasible at commercial scale.

421
422
423
424
425
426
427
428
429
430
431
432
433
434

Supplementary material

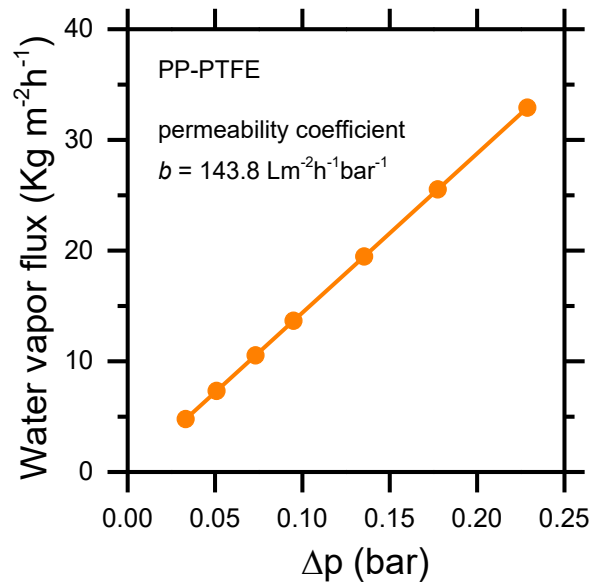
**Assessing the effect of feed temperature and cross-flow velocity on organic
fouling in membrane distillation using response surface methodology**

Francesco Ricceri^a, Bastiaan Blankert^b, Johannes S. Vrouwenvelder^b, Alberto Tiraferri^{a*}, Luca Fortunato^{b*}

^a Department of Environment, Land and Infrastructure Engineering (DIATI), Politecnico di Torino, Corso Duca degli Abruzzi 24, Turin, 10129, Italy

^b Water Desalination and Reuse Center (WDRC), King Abdullah University of Science and Technology (KAUST), Biological & Environmental Science & Engineering Division (BESE), Thuwal 23955-6900, Saudi Arabia

* Corresponding authors



435

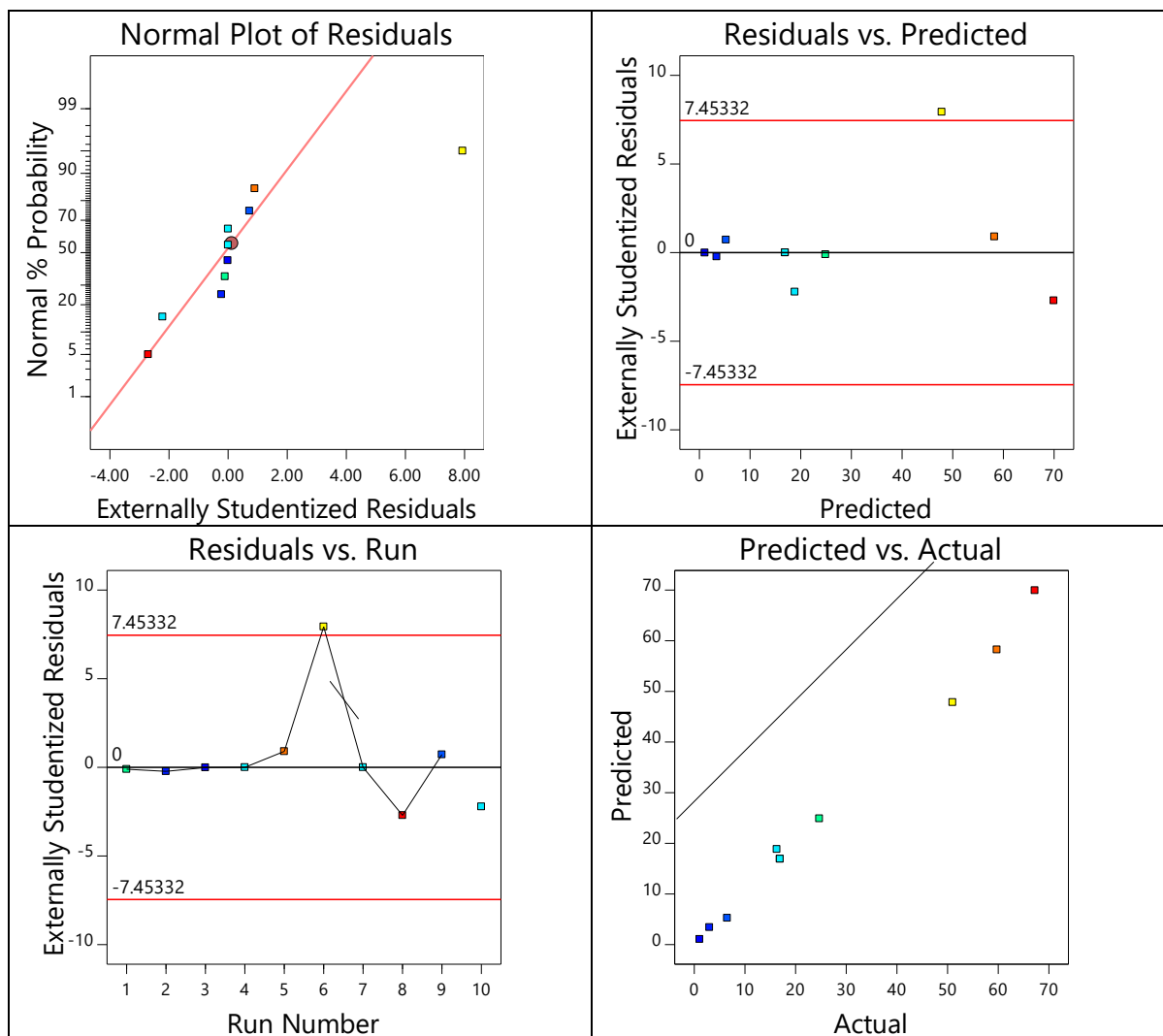
436 **Figure S.1.** Linear correlation between the obtained water vapor flux as a function of the
 437 applied vapor tension difference for the PP-PTFE membrane. The permeability, b , is
 438 reported.

439

440 **Table S.1.** List of the experiments suggested by Design Expert software for different
 441 combinations of cross-flow velocity and inlet feed temperature. Related experimental results
 442 for each response are also listed from the third column. C.P indicates the central point, a
 443 repetition of the 4th run, required by the software to retrieve a better model fitting.

Run	CFV	T_f	Initial flux decline	Final flux	Final thickness	J_w/J_0
-	m/s	$^{\circ}\text{C}$	$\text{Kg m}^{-2}\text{h}^{-1}/[-]$	$\text{Kg m}^{-2}\text{h}^{-1}$	μm	-
1	0.42	50.0	24.7	5.8	888	0.48
2	0.39	39.4	3.0	3.6	375	0.79
3	0.31	35.0	1.1	2.4	273	0.80
4	0.31	50.0	16.9	5.4	940	0.52
5	0.39	60.6	59.7	7.4	633	0.39
6	0.24	60.6	51.0	7.6	1066	0.42
7	0.31	65.0	67.2	7.6	1183	0.34
8	0.24	39.4	6.5	3.2	510	0.64
9	0.21	50.0	16.3	5.2	1000	0.47
C.P	0.31	50.0	17.6	5.1	920	0.57

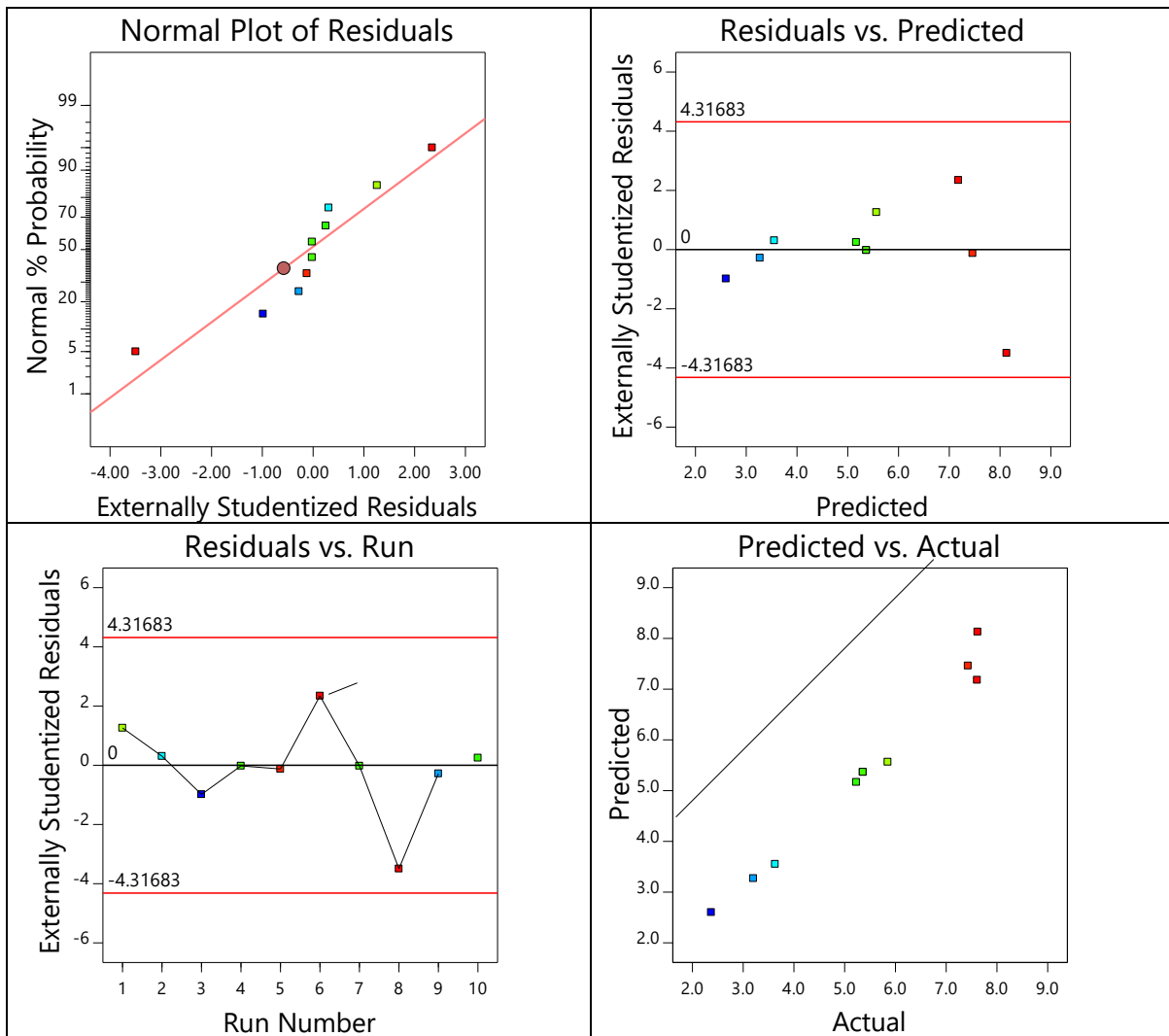
444



446

447 **Figure S.2.** Diagnostic plots for initial flux decline rate as response: (a) normal %
 448 probability vs. residuals; (b) residuals vs. predicted; (c) residuals vs. run order; (d) predicted
 449 vs. actual.

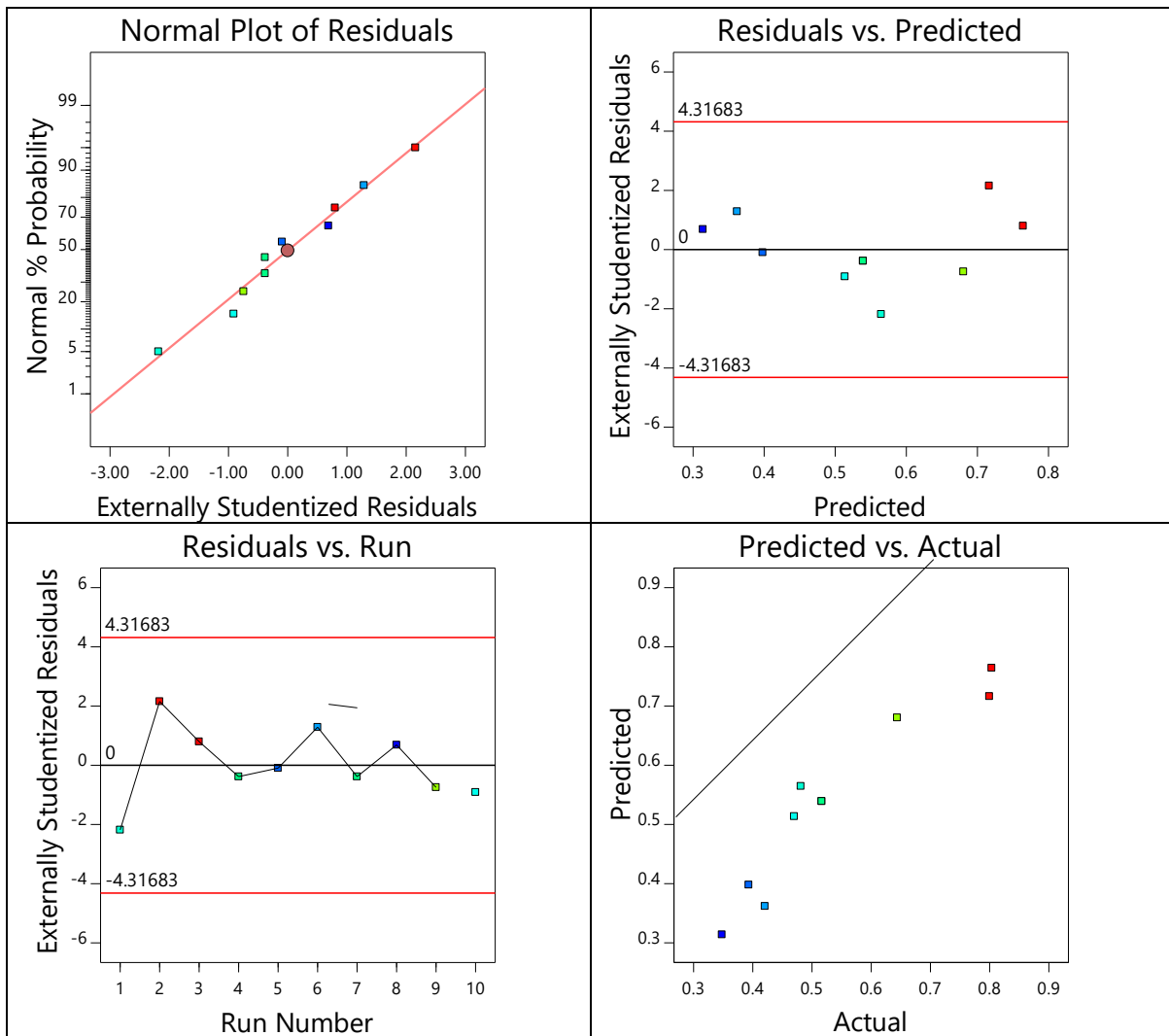
450



451

452 **Figure S.3.** Diagnostic plots for near-stable flux at the end of the test as response: (a) normal
 453 % probability vs. residuals; (b) residuals vs. predicted; (c) residuals vs. run order; (d)
 454 predicted vs. actual.

455



456

457 **Figure S.4.** Diagnostic plots for J_w/J_0 as response: (a) normal % probability vs. residuals; (b)
 458 residuals vs. predicted; (c) residuals vs. run order; (d) predicted vs. actual.

459

460 **Tab S.2.** Final equations computed by the statistical analysis and relating operating
 461 parameters to fouling behaviour. The equation can be used to make predictions about each
 462 response.

		Initial Flux decline	Final Flux	Final Thickness	J_w/J_0
		+206.19420	+5.37	+780.80	+1.21292
A-Cross flow velocity	*	-452.03539	+0.1409	-90.80	+0.243943
B-Feed temperature	*	-7.19720	+1.95	+262.62	-0.015014
AB	*	+3.90112			

A ²	*	+453.12607			
B ²	*	+0.082623			

463

464 **Appendix**

465 The model is generated for the four responses and is based on experimental data collected in
 466 the lab fitting a linear model for the final flux, final thickness, and final J_w/J_0 responses and a
 467 fitting a quadratic model for the initial flux decline rate response. The most general equation
 468 is reported here below:

$$y = \beta_0 + \sum_{k_i = 1} \beta_i x_i + \sum_{k_i = 1} \beta_{ii} x_i^2 + \sum_{k_j = i + 1} \beta_{ij} x_i x_j + \varepsilon$$

470 (Eq S.2)

471 where y is the predicted response, x represents the factors, k is the number of factors, β_0 is the
 472 constant coefficient, and β_i , β_{ii} , and β_{ij} are the regression coefficients of linear, quadratic, and
 473 interaction terms, respectively. To select the amount of experimental data to be collected,
 474 Central Composite Design (CCD) was applied. This design defines 2k corner points, 2k axial
 475 points, where k is the number of independent variables (or factors) selected, and a central
 476 point. In this study, two factors (Feed inlet temperature and feed cross-flow velocity) were
 477 selected. The number of experiments was directly calculated by the software according to the
 478 equation $n = 2^k \cdot 2k + Cp$, resulting in a total of 10 experiments, one of them represented by
 479 the central point (Cp). These test are a combination of different factors levels defined by the
 480 coded values calculated by applying the formulas in Table S2. The coded value associated
 481 with α is representative of the rotatability of the model which suggested Practical alpha due to
 482 $k < 6$ and equal to 1,41, which represents the distance.

483

484

Table S2. Coded and un-coded values for CCD

Coded value	Un-coded value
$-\alpha$	X_{min}
-1	$\frac{(\alpha - 1)X_{max} + (\alpha + 1)X_{min}}{2\alpha}$
0	$\frac{X_{max} + X_{min}}{2}$
+1	$\frac{(\alpha - 1)X_{min} + (\alpha + 1)X_{max}}{2\alpha}$
$+\alpha$	X_{max}

485

- 487 [1] N. Thomas, M.O. Mavukkandy, S. Loutatidou, H.A. Arafat, Membrane distillation research &
488 implementation: Lessons from the past five decades, *Separation and Purification Technology*, 189
489 (2017) 108-127.
- 490 [2] L.M. Camacho, L. Dumée, J. Zhang, J.-d. Li, M. Duke, J. Gomez, S. Gray, Advances in membrane
491 distillation for water desalination and purification applications, *Water*, 5 (2013) 94-196.
- 492 [3] I. Hitsov, L. Eykens, W. De Schepper, K. De Sitter, C. Dotremont, I. Nopens, Full-scale direct
493 contact membrane distillation (DCMD) model including membrane compaction effects, *Journal of*
494 *membrane science*, 524 (2017) 245-256.
- 495 [4] G. Dong, J.F. Kim, J.H. Kim, E. Drioli, Y.M. Lee, Open-source predictive simulators for scale-up of
496 direct contact membrane distillation modules for seawater desalination, *Desalination*, 402 (2017)
497 72-87.
- 498 [5] H. Susanto, Towards practical implementations of membrane distillation, *Chemical Engineering*
499 *and Processing: Process Intensification*, 50 (2011) 139-150.
- 500 [6] M. Khayet, T. Matsuura, *Membrane distillation: principles and applications*, (2011).
- 501 [7] B. Ashoor, S. Mansour, A. Giwa, V. Dufour, S. Hasan, Principles and applications of direct contact
502 membrane distillation (DCMD): a comprehensive review, *Desalination*, 398 (2016) 222-246.
- 503 [8] T. Horseman, Y. Yin, K.S. Christie, Z. Wang, T. Tong, S. Lin, Wetting, scaling, and fouling in
504 membrane distillation: State-of-the-art insights on fundamental mechanisms and mitigation
505 strategies, *ACS ES&T Engineering*, 1 (2020) 117-140.
- 506 [9] M. Rezaei, D.M. Warsinger, M.C. Duke, T. Matsuura, W.M. Samhaber, Wetting phenomena in
507 membrane distillation: Mechanisms, reversal, and prevention, *Water research*, 139 (2018) 329-352.
- 508 [10] E. Guillen-Burrieza, M. Mavukkandy, M. Bilad, H. Arafat, Understanding wetting phenomena in
509 membrane distillation and how operational parameters can affect it, *Journal of Membrane Science*,
510 515 (2016) 163-174.
- 511 [11] S. Shao, D. Shi, J. Hu, W. Qing, X. Li, X. Li, B. Ji, Z. Yang, H. Guo, C.Y. Tang, Unraveling the Kinetics
512 and Mechanism of Surfactant-Induced Wetting in Membrane Distillation: An In Situ Observation with
513 Optical Coherence Tomography, *Environmental science & technology*, (2021).
- 514 [12] D. Hou, Z. Yuan, M. Tang, K. Wang, J. Wang, Effect and mechanism of an anionic surfactant on
515 membrane performance during direct contact membrane distillation, *Journal of Membrane Science*,
516 595 (2020) 117495.
- 517 [13] K.S. Christie, Y. Yin, S. Lin, T. Tong, Distinct behaviors between gypsum and silica scaling in
518 membrane distillation, *Environmental science & technology*, 54 (2019) 568-576.
- 519 [14] M. Gryta, Fouling in direct contact membrane distillation process, *Journal of membrane science*,
520 325 (2008) 383-394.
- 521 [15] P. Wang, T.-S. Chung, Recent advances in membrane distillation processes: Membrane
522 development, configuration design and application exploring, *Journal of membrane science*, 474
523 (2015) 39-56.
- 524 [16] F. Ricceri, M. Giagnorio, G. Farinelli, G. Blandini, M. Minella, D. Vione, A. Tiraferri, Desalination
525 of produced Water by Membrane Distillation: Effect of the feed components and of a pre-treatment
526 by fenton oxidation, *Scientific reports*, 9 (2019) 1-12.
- 527 [17] L. Fortunato, H. Elcik, B. Blankert, N. Ghaffour, J. Vrouwenvelder, Textile dye wastewater
528 treatment by direct contact membrane distillation: Membrane performance and detailed fouling
529 analysis, *Journal of Membrane Science*, 636 (2021) 119552.
- 530 [18] J. Guo, L. Fortunato, B.J. Deka, S. Jeong, A.K. An, Elucidating the fouling mechanism in
531 pharmaceutical wastewater treatment by membrane distillation, *Desalination*, 475 (2020) 114148.
- 532 [19] J.-G. Lee, Y. Jang, L. Fortunato, S. Jeong, S. Lee, T. Leiknes, N. Ghaffour, An advanced online
533 monitoring approach to study the scaling behavior in direct contact membrane distillation, *Journal of*
534 *Membrane Science*, 546 (2018) 50-60.

535 [20] A. Abdel-Karim, S. Leaper, C. Skuse, G. Zaragoza, M. Gryta, P. Gorgojo, Membrane cleaning and
536 pretreatments in membrane distillation-a review, *Chemical Engineering Journal*, (2021) 129696.

537 [21] C.A. Robbins, Y. Yin, A.J. Hanson, J. Blotevogel, T. Borch, T. Tong, Mitigating membrane wetting
538 in the treatment of unconventional oil and gas wastewater by membrane distillation: A comparison
539 of pretreatment with omniphobic membrane, *Journal of Membrane Science*, (2021) 120198.

540 [22] G. Naidu, S. Jeong, S.-J. Kim, I.S. Kim, S. Vigneswaran, Organic fouling behavior in direct contact
541 membrane distillation, *Desalination*, 347 (2014) 230-239.

542 [23] F. Wendland, A. Blum, M. Coetsiers, R. Gorova, J. Griffioen, J. Grima, K. Hinsby, R. Kunkel, A.
543 Marandi, T. Melo, European aquifer typology: a practical framework for an overview of major
544 groundwater composition at European scale, *Environmental Geology*, 55 (2008) 77-85.

545 [24] R. Valladares Linares, L. Fortunato, N. Farhat, S. Bucs, M. Staal, E. Fridjonsson, M. Johns, J.S.
546 Vrouwenvelder, T. Leiknes, Mini-review: novel non-destructive in situ biofilm characterization
547 techniques in membrane systems, *Desalination and Water Treatment*, 57 (2016) 22894-22901.

548 [25] L. Fortunato, A.F. Lamprea, T. Leiknes, Evaluation of membrane fouling mitigation strategies in
549 an algal membrane photobioreactor (AMPBR) treating secondary wastewater effluent, *Science of
550 The Total Environment*, 708 (2020) 134548.

551 [26] L. Fortunato, Y. Jang, J.-G. Lee, S. Jeong, S. Lee, T. Leiknes, N. Ghaffour, Fouling development in
552 direct contact membrane distillation: Non-invasive monitoring and destructive analysis, *Water
553 research*, 132 (2018) 34-41.

554 [27] F. Ricceri, G. Farinelli, M. Giagnorio, A. Zamboi, A. Tiraferri, Optimization of physico-chemical
555 and membrane filtration processes to remove high molecular weight polymers from produced water
556 in enhanced oil recovery operations, *Journal of Environmental Management*, 302 (2022) 114015.

557 [28] I. Righetto, R.A. Al-Juboori, J.U. Kaljunen, A. Mikola, Multipurpose treatment of landfill leachate
558 using natural coagulants—Pretreatment for nutrient recovery and removal of heavy metals and
559 micropollutants, *Journal of Environmental Chemical Engineering*, 9 (2021) 105213.

560 [29] I. Righetto, R.A. Al-Juboori, J.U. Kaljunen, A. Mikola, Wastewater treatment with starch-based
561 coagulants for nutrient recovery purposes: Testing on lab and pilot scales, *Journal of Environmental
562 Management*, 284 (2021) 112021.

563 [30] M. Ahmadi, F. Vahabzadeh, B. Bonakdarpour, E. Mofarrah, M. Mehranian, Application of the
564 central composite design and response surface methodology to the advanced treatment of olive oil
565 processing wastewater using Fenton's peroxidation, *Journal of Hazardous Materials*, 123 (2005) 187-
566 195.

567 [31] T. Rakić, I. Kasagić-Vujanović, M. Jovanović, B. Jančić-Stojanović, D. Ivanović, Comparison of full
568 factorial design, central composite design, and box-behnken design in chromatographic method
569 development for the determination of fluconazole and its impurities, *Analytical Letters*, 47 (2014)
570 1334-1347.

571 [32] M. Shokrollahi, M. Rezakazemi, M. Younas, Producing water from saline streams using
572 membrane distillation: modeling and optimization using CFD and design expert, *International Journal
573 of Energy Research*, 44 (2020) 8841-8853.

574 [33] S. Srisurichan, R. Jiraratananon, A. Fane, Humic acid fouling in the membrane distillation
575 process, *Desalination*, 174 (2005) 63-72.

576 [34] G. Naidu, S. Jeong, S. Vigneswaran, Influence of feed/permeate velocity on scaling development
577 in a direct contact membrane distillation, *Separation and Purification Technology*, 125 (2014) 291-
578 300.

579 [35] S. Al-Obaidani, E. Curcio, F. Macedonio, G. Di Profio, H. Al-Hinai, E. Drioli, Potential of membrane
580 distillation in seawater desalination: thermal efficiency, sensitivity study and cost estimation, *Journal
581 of membrane science*, 323 (2008) 85-98.

582 [36] F.A. Banat, J. Simandl, Theoretical and experimental study in membrane distillation,
583 *Desalination*, 95 (1994) 39-52.

584 [37] G.W. Thomson, The Antoine equation for vapor-pressure data, *Chemical reviews*, 38 (1946) 1-
585 39.

586 [38] C. Boo, S. Hong, M. Elimelech, Relating organic fouling in membrane distillation to
587 intermolecular adhesion forces and interfacial surface energies, *Environmental science &*
588 *technology*, 52 (2018) 14198-14207.

589 [39] A. Alkhatib, M.A. Ayari, A.H. Hawari, Fouling mitigation strategies for different foulants in
590 membrane distillation, *Chemical Engineering and Processing-Process Intensification*, 167 (2021)
591 108517.

592 [40] A. Hausmann, P. Sancio, T. Vasiljevic, M. Weeks, K. Schroën, S. Gray, M. Duke, Fouling
593 mechanisms of dairy streams during membrane distillation, *Journal of Membrane Science*, 441
594 (2013) 102-111.

595 [41] R.W. Field, G.K. Pearce, Critical, sustainable and threshold fluxes for membrane filtration with
596 water industry applications, *Advances in colloid and interface science*, 164 (2011) 38-44.

597 [42] T.-T. Nguyen, C. Lee, R.W. Field, I.S. Kim, Insight into organic fouling behavior in polyamide thin-
598 film composite forward osmosis membrane: Critical flux and its impact on the economics of water
599 reclamation, *Journal of Membrane Science*, 606 (2020) 118118.

600 [43] F. Ricceri, M. Giagnorio, K.R. Zodrow, A. Tiraferri, Organic fouling in forward osmosis: Governing
601 factors and a direct comparison with membrane filtration driven by hydraulic pressure, *Journal of*
602 *Membrane Science*, 619 (2021) 118759.

603 [44] M. Laqbaqbi, M. García-Payo, M. Khayet, J. El Kharraz, M. Chaouch, Application of direct contact
604 membrane distillation for textile wastewater treatment and fouling study, *Separation and*
605 *Purification Technology*, 209 (2019) 815-825.

606 [45] J. Ortiz de Zárate, C. Rincón, J. Mengual, Concentration of bovine serum albumin aqueous
607 solutions by membrane distillation, *Separation science and technology*, 33 (1998) 283-296.

608 [46] S. Srisurichan, R. Jiratananon, A. Fane, Mass transfer mechanisms and transport resistances in
609 direct contact membrane distillation process, *Journal of membrane science*, 277 (2006) 186-194.

610 [47] L. Eykens, I. Hitsov, K. De Sitter, C. Dotremont, L. Pinoy, I. Nopens, B. Van der Bruggen, Influence
611 of membrane thickness and process conditions on direct contact membrane distillation at different
612 salinities, *Journal of Membrane Science*, 498 (2016) 353-364.

613 [48] M.S. Toran, A. D'Haese, I. Rodríguez-Roda, W. Gernjak, Fouling propensity of novel TFC
614 membranes with different osmotic and hydraulic pressure driving forces, *Water Research*, 175
615 (2020) 115657.

616 [49] F.A. Siddiqui, Q. She, A.G. Fane, R.W. Field, Exploring the differences between forward osmosis
617 and reverse osmosis fouling, *Journal of Membrane Science*, 565 (2018) 241-253.

618 [50] N. Biglarijoo, S.A. Mirbagheri, M. Ehteshami, S.M. Ghaznavi, Optimization of Fenton process
619 using response surface methodology and analytic hierarchy process for landfill leachate treatment,
620 *Process Safety and Environmental Protection*, 104 (2016) 150-160.

621 [51] H. Pashaei, A. Ghaemi, M. Nasiri, B. Karami, Experimental modeling and optimization of CO₂
622 absorption into piperazine solutions using RSM-CCD methodology, *ACS omega*, 5 (2020) 8432-8448.

623 [52] M. Qtaishat, T. Matsuura, B. Kruczek, M. Khayet, Heat and mass transfer analysis in direct
624 contact membrane distillation, *Desalination*, 219 (2008) 272-292.

625 [53] Z. Ding, L. Liu, Z. Liu, R. Ma, Fouling resistance in concentrating TCM extract by direct contact
626 membrane distillation, *Journal of Membrane Science*, 362 (2010) 317-325.

627 [54] A. Hausmann, P. Sancio, T. Vasiljevic, U. Kulozik, M. Duke, Performance assessment of
628 membrane distillation for skim milk and whey processing, *Journal of Dairy Science*, 97 (2014) 56-71.

629 [55] M. Laqbaqbi, J.A. Sanmartino, M. Khayet, C. García-Payo, M. Chaouch, Fouling in membrane
630 distillation, osmotic distillation and osmotic membrane distillation, *Applied Sciences*, 7 (2017) 334.

631